Mixed Rayleigh-Stoneley modes: Analysis of seismic waveguide coupling and sensitivity to lower-mantle structures

Harry Matchette-Downes[1], Jia Shi[2], Jingchen Ye[2], Jiayuan Han[2], Robert D van der Hilst[1], and Maarten V de Hoop[2]

[1]Massachusetts Institute of Technology
[2]Rice University

November 22, 2022

Abstract

A better understanding of Earth's core-mantle boundary (CMB) region is required to address major questions about our planet's internal dynamics, magnetic field, and thermal evolution. Valuable constraints have come from observations of (CMB-) Stoneley modes, a class of seismic free oscillation whose displacement decreases away from the solid-fluid boundary. The high-frequency modes that are most sensitive to the CMB region are too localized there to be observed at Earth's surface. Here we clarify why some higher-frequency Stoneley modes can be detected: via 'mixing' with surface-localized Rayleigh-type modes of similar frequency. We examine the concept of mixed Rayleigh-Stoneley modes analytically and with a finite-element method. Our calculations show that mixed modes are a sensitive probe of radial and lateral variations in material properties near the CMB. More generally, 'seismic waveguide coupling' could help to characterize systems ranging from cell membranes to Pluto's lithosphere.

Mixed Rayleigh-Stoneley modes: Analysis of seismic waveguide coupling and sensitivity to lower-mantle structures

Harry Matchette-Downes[1], Jia Shi[2*], Jingchen Ye[3,4†], Jiayuan Han[2], Robert D. van der Hilst[1], Maarten V. de Hoop[2,3]

[1]Department of Earth, Atmospheric and Planetary Sciences, Massachusetts Institute of Technology, 77 Massachusetts Avenue, MA 02139, U.S.A.

[2]Department of Earth, Environmental and Planetary Sciences, Rice University, 6100 Main Street, TX 77005, U.S.A.

[3]Department of Computational and Applied Mathematics, Rice University, 6100 Main Street, TX 77005, U.S.A.

[4]Applied Physics Program, Rice University, 6100 Main Street, TX 77005, U.S.A.

Key Points:

- Parallel seismic waveguides become coupled when wave frequencies are similar, which only occurs close to dispersion branch crossings.
- Waveguide coupling of Rayleigh and (core–mantle-boundary) Stoneley modes allows a few higher-frequency 'mixed' modes to be observed.
- Direct 3-D mode calculations show how the splitting of these few mixed modes contains detailed information about lowermost mantle structures.

*Now at: Shell International Exploration and Production Inc.

†Now at: Google LLC.

Corresponding author: Harry Matchette-Downes, hrmd@mit.edu

Abstract

A better understanding of Earth's core-mantle boundary (CMB) region is required to address major questions about our planet's internal dynamics, magnetic field, and thermal evolution. Valuable constraints have come from observations of (CMB-) Stoneley modes, a class of seismic free oscillation whose displacement decreases away from the solid-fluid boundary. The high-frequency modes that are most sensitive to the CMB region are too localized there to be observed at Earth's surface. Here we demonstrate that waveguide coupling of Rayleigh and CMB Stoneley modes allows some higher-frequency 'mixed' Stoneley modes to be observed. We examine the concept of mixed Rayleigh-Stoneley modes analytically and with a finite-element method. Our calculations show that mixed modes are a sensitive probe of radial and lateral variations in material properties near the CMB. More generally, 'seismic waveguide coupling' could help to characterize systems ranging from cell membranes to Pluto's lithosphere.

Plain-language summary

After a large earthquake, Earth 'rings like a bell' for days due to constructive interference of seismic waves. The frequencies of these 'normal mode' oscillations provide information about Earth's internal structure, including some of the best constraints on density variations. Observations of 'Stoneley modes', whose motion is largest near the core-mantle boundary, help to assess various hypotheses in solid-Earth geophysics. However, only low-frequency Stoneley modes are observable at the surface, limiting the resolution of models of the CMB region. We show that these limitations can be overcome at certain frequencies where the Stoneley modes 'mix' with 'Rayleigh modes', whose motion is largest at Earth's surface. In these special cases, relatively high-frequency Stoneley modes can be excited by earthquakes, detected by seismometers, and used to study the lower mantle. Additionally, such coupling between seismic 'waveguides' is expected in many other settings, from cells to ice sheets.

1 Introduction

Improvements in models of the density field near Earth's core-mantle boundary (CMB) would enhance our understanding of Earth's history, mantle dynamics, and outer-core stratification. Key constraints come from studies of seismic normal modes. One of the major conclusions of such studies has been that the lower mantle's so-called large low-

shear-velocity provinces (LLSVPs) are also high-density provinces (Ishii & Tromp, 1999; Trampert et al., 2004; Mosca et al., 2012; Moulik & Ekström, 2016), in agreement with geodynamical arguments regarding their stability (e.g. Kellogg et al., 1999) and recent work using 'tidal tomography' (Lau et al., 2017).

However, some have questioned the conclusions based on normal-mode observations. Only low-frequency modes (below around 5 mHz) show significant sensitivity to density, because they have non-negligible self-gravitation (Kennett, 1998). These low-frequency modes tend to have significant displacement throughout the mantle, leading to poor radial resolution and trade-offs between parameters in different parts of the Earth (Resovsky & Ritzwoller, 1999). It seems difficult to resolve these trade-offs without prior assumptions (Resovsky & Ritzwoller, 1999; Romanowicz, 2001).

Recently, normal-mode researchers have attempted to overcome the trade-offs by including modes which are localized near the CMB, known as Stoneley modes (Koelemeijer et al., 2013, 2015, illustrated in Fig. 1a,b). These modes are quite sensitive to density, due to self-gravitation caused by the large CMB density contrast. Koelemeijer et al. (2017) fitted these observations (as part of a mode catalog) and proposed that the LLSVPs are lighter-than-average anomalies, in contrast with previous workers.

However, even Stoneley modes have substantial displacement throughout the mantle at lower frequencies (Fig. 1a), so they still suffer from significant trade-offs. Ideally, one would use the sharply-localized higher-frequency Stoneley modes, but these are not usually observable at the surface (Fig. 1b). In this paper, we explore how some higher-frequency Stoneley modes have been observed at the surface, not in a pure form, but through 'mixing' (or 'hybridizing') with surface-localized Rayleigh modes at certain frequencies (Fig. 1c).

This understanding, combined with more comprehensive observations of these mixed Rayleigh-Stoneley modes, could tighten constraints on structures in the lowermost mantle. Such constraints are crucial for understanding geodynamics (see review by Tackley, 2012), including the role of post-perovskite (Koelemeijer et al., 2018), Earth's formation and thermal history (e.g. Zhang & Zhong, 2011) and the heat budget for the geodynamo (Buffett, 2002; Aubert et al., 2008; Lay et al., 2008). It might also be possible to constrain the radial stratification of the outer core (see review by Hirose et al., 2013), although the sensitivity of Stoneley modes to the highly inhomogeneous lower mantle makes this difficult (Irving et al., 2018).

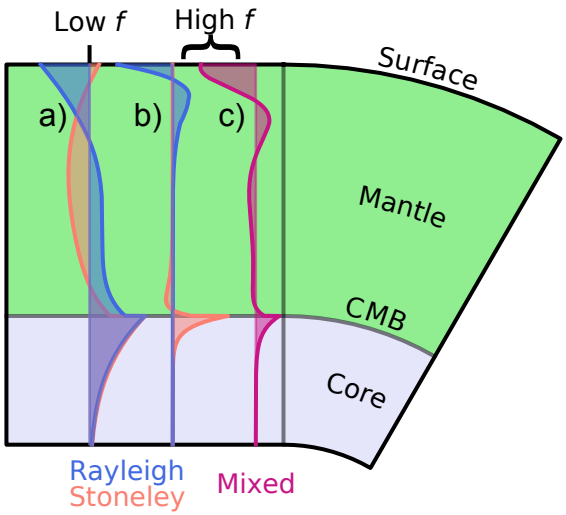

Figure 1. Illustration of typical mode displacement patterns, showing differences between high- and low-frequency modes, and between Rayleigh and Stoneley modes, and the unique mixed modes. Spherical and planar systems are shown side-by-side, and the displacement patterns shown are qualitatively the same for both systems.

All of these interpretations of seismic data require a way of solving the forward problem. The normal-mode method is well-suited to low-frequency applications and has the advantage that once the modes are computed, changing the source in simulations can be accomplished at very low cost, unlike, for example, with a spectral-element method (Komatitsch & Tromp, 2002). Unfortunately, the standard numerical-integration method for calculating the modes of a spherically-symmetric planet cannot be easily generalised to three dimensions. Instead, the 3-D problem is approached using the 1-D solution as a basis, as in conventional perturbation theory (Dahlen & Tromp, 1998) and the direct-solution method (Al-Attar et al., 2012). These approaches work well at low frequencies, but the accuracy of the perturbation assumption has not been tested. In this study, we demonstrate a normal-mode technique which works in one and three dimensions, and does not require any perturbation assumption.

Another advantage of the normal-mode approach is that modes provide physical insight (e.g. Lau et al., 2016), as we discuss in this study. Related to this, the normal-mode formalism is well-suited to the inverse problem, because it leads directly to the requisite frequency and sensitivity information. In some situations, especially the burgeoning field of planetary seismology, data coverage may be limited and amplitude informa-

tion may not be available; in this case it is helpful that normal-mode centre frequencies are almost independent of the source term.

2 Methods

2.1 Calculation of the modes of a spherically-symmetric planet

We first calculated the spheroidal (P–SV-polarized) modes of a spherically-symmetric non-rotating Earth model using the *Ouroboros* code (Ye, 2018; Shi et al., 2019, `https://github.com/harrymd/Ouroboros`). We included the effect of gravity but neglected perturbations to the gravitational potential. We used the isotropic mean of the PREM Earth model (Dziewonski & Anderson, 1981), at a period of 1 s, with no attenuation. The first layer (water) was replaced by a solid layer matching the second layer.

2.2 Analysis and calculation of surface waves in a half-space

To understand the behavior of the mixed Rayleigh-Stoneley modes, we sought high-frequency solutions to the equations of motion for interface waves propagating horizontally through a solid, stratified layer overlying a fluid half-space, as described in detail by Ye (2018). First, we separated the P-SV from the SH equations. We then rewrote the P-SV equations in terms of the P and SV eigenfunctions, and solved them in the high-frequency ('asymptotic') limit by following the approach of Woodhouse (1978). Finally, we used the WKB approximation to find expressions for the P and SV wavefunctions. In this step, we followed the approach of Alenitsyn (1998), who considered a stratified fluid layer over a solid half-space. We combined this asymptotic solution with the boundary conditions to yield an analytical dispersion equation.

To verify the applicability the high-frequency analysis to the modes of our spherical Earth model, we calculated Rayleigh and Stoneley dispersion curves for 'flattened' equivalent of the modified PREM model. For this we used the *Computer Programs in Seismology* software package (CPS; Herrmann, 2013) which implements the Haskell-Thomson propagator matrix technique (Haskell, 1964; C. Y. Wang & Herrmann, 1980). In this code the Earth-flattening transform is based on the work of Biswas and Knopoff (1970), Biswas (1972) and Chapman (1973).

2.3 Calculation of the modes of a laterally-heterogeneous planet

Finally, we calculated the modes of a 3-D Earth model containing a hypothetical LLSVP using the same technique as in the spherically-symmetric case. In three dimensions this is implemented as the *NormalModes* code (Shi et al., 2018, 2019). Starting from our spherically-symmetric modified PREM model, we built a 3-D mesh consisting of around 2.5 million second-order tetrahedral finite elements. We then added a representative LLSVP to the base of the mantle.

Significant uncertainty exists regarding the material properties of LLSVPs, as well as their composition, temperature and geometry (see review by Lay, 2015). For the illustration of the concepts introduced here, we chose properties of the model LLSVP within the published range of observations. Specifically, the LLSVP extends from the CMB up to a uniform thickness of 400 km, based on the lower bound in the study of Y. Wang and Wen (2007). We use the outline of the African LLSVP at 2700 km depth from the consensus study of Cottaar and Lekić (2016). We used an S-wave-speed anomaly of $-4\,\%$. Using the ratio of S- and P-wave-speed anomalies from Tkalčić and Romanowicz (2002) of 2.5, we then chose the P-wave-speed anomaly to be $-1.6\,\%$. We took a density anomaly of $+1\,\%$ (Ishii & Tromp, 1999; Moulik & Ekström, 2016), although others, such as Romanowicz (2001), argue that the density anomaly could be positively correlated to the S-wave-speed anomaly.

3 Results

3.1 Mixed modes of a spherical Earth

The calculated frequencies of the spheroidal modes are plotted on a 'dispersion diagram' (relating frequency and wavelength) in Fig. 2a. The Stoneley modes form a line which has a steeper slope than the Rayleigh-mode overtone, indicative of a higher group velocity, so that there are a series of 'quasi-intersections' or 'avoided crossings', the first two of which are outlined by boxes. We focus first on the modes of the second quasi-intersection (Fig. 2b).

The vertical-component displacement eigenfunctions of these modes (as a function of radius) are shown in Fig. 3a,b. These two panels show the upper and lower branches, respectively, and each shows a progression of four modes along the branch, as labeled in Fig. 2b, from lowest to highest frequency. The lower branch (Fig. 3a) shows a tran-

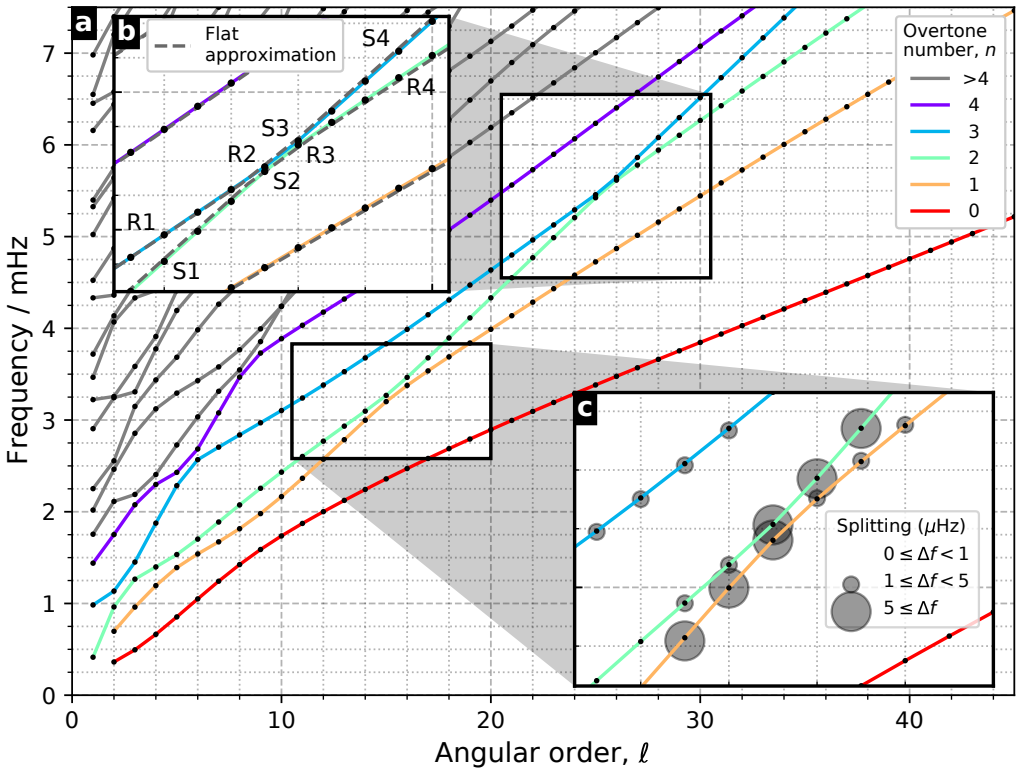

Figure 2. Dispersion diagrams of Earth's low-frequency spheroidal modes (black dots), relating angular order (ℓ) and frequency, with lines connecting branches of constant overtone number (n). (The angular order of a mode controls the total number of nodal planes in the displacement pattern. For a given value of ℓ, modes are assigned a value of n in order of increasing frequency. A spheroidal mode with these two numbers is denoted ${}_n\mathrm{S}_l$. For surface-wave equivalent modes with large ℓ and small n, the angular order is related to the wavelength (λ) by $\ell \approx 2\pi R/\lambda$ where R is the radius of the planet.) a) Overview. b) The second-quasi intersection, overlaid with the half-space approximation. The labeled Rayleigh (R1, ..., R4) and Stoneley (S1, ..., S4) modes have their radial displacement patterns plotted in Fig. 3a,b. c) The first quasi-intersection, showing the splitting of each mode due to lowermost-mantle heterogeneity, as detailed in Fig. 4.

sition from a pure Stoneley mode (S1), with much larger displacement near the core-mantle boundary, to a pure Rayleigh mode (R4) with much larger displacement near the surface. The intermediate modes (S2 and R3) have significant displacement at both interfaces. We identify these as 'mixed Stoneley-Rayleigh modes'. The same behavior is seen in the upper branch (Fig. 3b), except that the transition is from a Rayleigh mode (R1) to a Stoneley mode (S4). Note that the mixed modes pairs (e.g. S2 and R2) are not the result of 'coupling' in the usual mode-seismology sense, where 'coupling' is attributed to aspherical structure, but arise from the interaction of wave phenomena at separate (parallel) interfaces, even a spherically-symmetrical medium with no lateral heterogeneity.

The displacement patterns have zero crossings, which, like all evanescent waves, shift away from an interface when the frequency decreases, and vice versa. This effect is shown in the inset in Fig. 3d. The small shifts demonstrate that the dramatic change in mode character, from Rayleigh to Stoneley, occurs over a small frequency range.

A gallery of additional examples (Supplement S5; includes tangential component) shows that mixing occurs near other Stoneley-Rayleigh quasi-intersections, although mixing becomes weaker and narrower at higher frequencies. At the lowest frequencies, all the modes of the CMB Stoneley branch could be described as mixed Stoneley-Rayleigh modes (recall Fig. 1a). The distinction between Rayleigh, Stoneley, and mixed modes gradually becomes clearer beyond the first intersection, with the second intersection being perhaps the best example (Fig. 3a,b). By the fourth quasi-intersection (around 11.5 mHz), only a single pair of modes is affected, and the mixing is negligible.

Some mixed Stoneley-Rayleigh modes have been previously observed in real data, where they are referred to simply as Stoneley modes (see the Discussion, section 4.1). We note that pure Stoneley modes cannot be excited by earthquakes, as earthquakes do not occur below depths of around 700 km. Even if a pure Stoneley mode were excited, it would not be detectable at the Earth's surface. In contrast, mixed modes can be excited by earthquakes and they can be detected at the surface. Their sensitivity is concentrated near the surface and CMB with little sensitivity to the mid-mantle.

Calculation of Stoneley modes is challenging for the commonly-used numerical integration approach (Dahlen & Tromp, 1998, page 312), for example as implemented in the *Mineos* library (Masters et al., 2011). The difficulty is that the boundary conditions must be applied at points of zero displacement. Mixed modes are doubly challenging be-

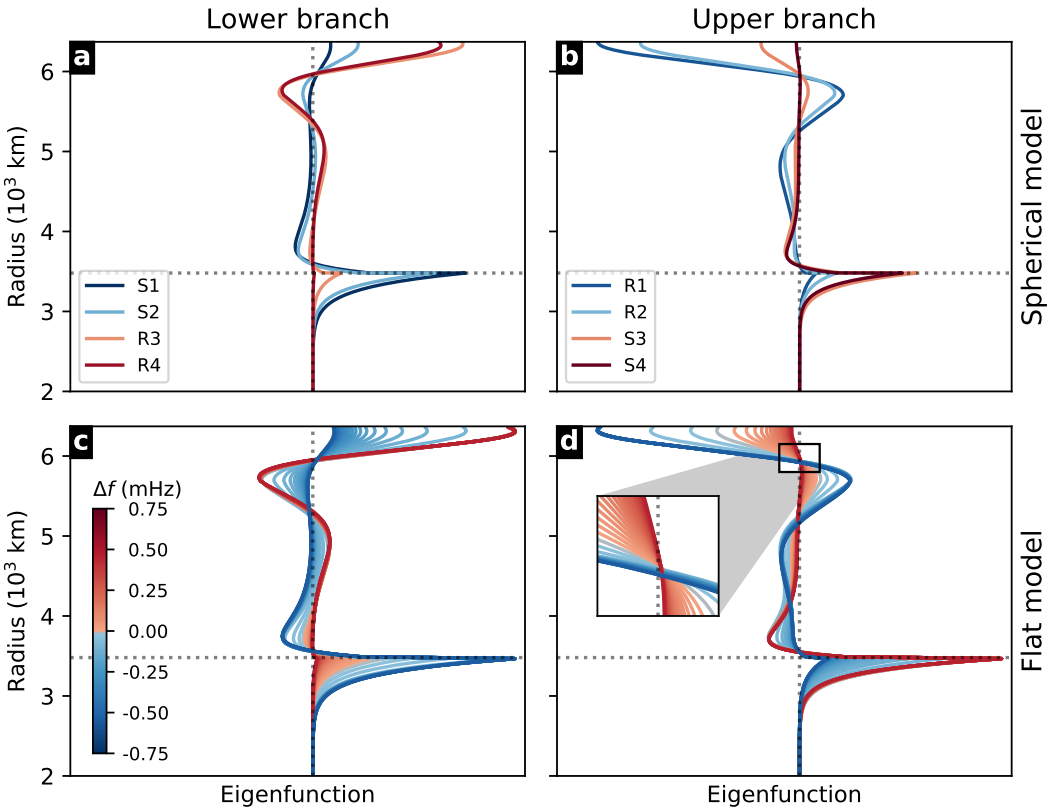

Figure 3. Profiles of vertical-component displacement as a function of radial coordinate, for modes along the quasi-intersecting mode branches shown in Fig. 2b, illustrating mode mixing and the correspondence between an infinite, flat system and a spherical one. Each profile is colored according to the frequency of the mode relative to the intersection frequency. Panels a) and b): Selected eigenfunctions calculated for a spherical Earth, as labeled in Fig. 2b. The displacement is multiplied by the radial coordinate, to allow proper comparison of particle displacements at each depth. Panels c) and d): The eigenfunctions of a half-space model, which vary smoothly as a function of frequency. The 'radius' here refers to the coordinate before flattening takes place. The relative amplitudes of different eigenfunctions have no physical meaning; only their shape is important.

cause it is hard to guarantee orthogonality in the case of the near-identical frequencies ('accidental degeneracy'). Our finite-element technique does not encounter these difficulties. However, we find that the frequencies, eigenfunctions (and therefore sensitivity kernels) are indistinguishable between the *Ouroboros* and *Mineos* codes when the starting model has an appropriate reference frequency.

In conclusion, the calculated mode displacement patterns (Fig. 3a,b) thus show that Stoneley and Rayleigh modes mix when they are close in frequency, creating mixed Stoneley-Rayleigh modes, which should be excitable, observable and sensitive to the deep mantle.

3.2 Coupled waveguides in a flat system

Our high-frequency analytical solution (Methods, section 2.2) separates in most cases to Rayleigh waves at the solid-vacuum interface (Strutt, 1885) and Stoneley waves at the solid-fluid interface (Stoneley, 1924; Scholte, 1942), with the allowed combinations of frequency and wavelength governed by two dispersion curves. (Dispersion curves are the continuous analog of the discrete dispersion diagram shown in Fig. 2.) However, near the quasi-intersection point, the two solutions cannot be separated, and the dispersion equation has two roots, one either side of the intersection point. This explains why there is a quasi-intersection instead of a true intersection. This behavior was previously pointed out by Zhao and Dahlen (1993), who noted from Arnold (1978, pages 425–437) that 'such avoided crossings are characteristic of weakly-coupled spectra in all physical systems'.

One of the pair of solutions has maximum displacement at the solid-fluid interface, but also non-negligible displacement at the free surface; we call this a 'mixed Stoneley-Rayleigh mode'. Conversely, the other root has maximum displacement at the free surface but non-negligible displacement at the fluid-solid interface; we call this a 'mixed Rayleigh-Stoneley mode' (although we use both terms loosely to refer to both kinds). If we consider the other side of the intersection, the two kinds of mode are interchanged. We also find that the portion of the dispersion diagram affected by the quasi-intersection becomes smaller as the frequency increases.

To relate this analysis to the spherical case, we calculated the dispersion curves and displacement patterns of an equivalent flattened Earth model (Methods, section 2.2), as shown in Fig. 2c and Fig. 3c,d. The fundamental difference between the flat and spherical systems is that the flat system has continuous solution curves (derivatives are shown

in Supplement S1) instead of discrete solution points. Apart from this, the flat model appears to be a good approximation of the spherical case. We do not expect perfect agreement, because of the approximations of the Earth-flattening calculations, and also because gravity is neglected. Nonetheless, their similarity suggests that, at these 'high' frequencies, qualitative insights from our analysis are also applicable to the spherical case, consistent with Woodhouse (1978), whose analysis we followed.

These results show that Stoneley-Rayleigh mixing occurs in infinite, flat systems, and is not a result of the finite size or curvature of planets. It is an example of what we identify as 'seismic waveguide coupling', which occurs between two waveguides whenever their dispersion curves come close to intersecting, in spite of a large physical separation. Our analysis predicts the properties suggested by the spherical calculations: the dispersion curves can never intersect (Fig. 2b,c), mode mixing occurs close to quasi-intersection points (Fig. 3), and the affected intersection region becomes narrower at higher frequencies (Supplement S5). Having established the existence and properties of Stoneley-Rayleigh mixed modes, we now return to a slightly more realistic model of the Earth, to illustrate how these modes provide useful constraints on the lower mantle.

3.3 Mixed modes of a laterally-inhomogeneous Earth

We calculated the modes of a 3-D Earth model containing an LLSVP (Methods, section 2.3). As expected, the lateral heterogeneity splits each spherically-symmetric $(2\ell + 1)$ degenerate 'mode' (Fig. 2a) into a 'multiplet' with a range of frequencies, allowing a forensic analysis of the structure causing the splitting. The frequency splitting near the first quasi-intersection is shown in Fig. 2c, as the difference between the minimum and maximum frequencies of each multiplet. We see that the Stoneley modes and mixed Stoneley-Rayleigh modes are more severely split by the anomaly, confirming that they are unusually sensitive to the lowermost mantle. This illustrates how observations of the splitting of these modes provides tighter constraints on lower-mantle structures than observations of other modes.

A detailed view of the splitting is shown in Fig. 4a for the four modes nearest the quasi-intersection. The severity of the splitting varies between multiplets (as was already seen in Fig. 2c). This is because some of the multiplets are more sensitive to the CMB (for example, compare the sensitivity kernels for modes ${}_1S_{16}$ and ${}_2S_{16}$ in the gallery, Supplement S5). The $2\ell+1$ modes in each multiplet (31 or 33 for these four modes) show

irregular changes in frequency. We can understand how this splitting pattern arises by looking at the displacement patterns of some of the modes (Fig. 4b,c,d) of the most severely split multiplet ($_2S_{16}$).

The displacement patterns are shown for three of the 33 modes from the $_2S_{16}$ multiplet. We have chosen the modes with the highest, middle, and lowest frequencies, as indicated by the lines from panel a. For simplicity, we only show one component of the displacement (the radial component), and this component is only plotted at the CMB, where the displacement is at a maximum. The full displacement pattern for each mode (not shown here) is a three-dimensional vector field with both radial and tangential components.

The first observation of the displacement patterns is that the shape of the anomaly (indicated by a gray outline), along with the requirement that the modes are orthogonal, controls the 'shape' of the modes. Thus the modes form a series from high to low frequency. For our choice of material parameters, this sequence starts from the mode most concentrated within the anomaly (Fig. 4b) and ends with the mode least concentrated within the anomaly (Fig. 4d). This can be interpreted simply in terms of interfering waves traveling more slowly through the anomaly. In real observations, the individual singlets are usually blurred together, but a seismometer situated directly above the LLSVP would observe a lower frequency for mode $_2S_{16}$. The geographic and frequency variations across a mode multiplet are commonly summarized using a 'splitting function' map.

We note that displacement patterns at other depths (not shown here) are almost identical, except that they vary in amplitude. This is consistent with the unperturbed case, in which the normal modes can be separated into a product of a function of angular location and a function of radius. This latter function, the variation in displacement with radius, is shown for one mode in Fig. 4e. (More precisely, we plot the radial and consoidal spherical harmonic components with $m = 3$, the dominant value of m, but all values of m show the same pattern.) As shown by the dotted line, the perturbed result closely matches the result for the spherical Earth. This suggests that perturbed modes are predominantly a linear combination of modes within the same unperturbed multiplet (which have the same radial profiles), consistent with the 'isolated multiplet' approximation commonly used in perturbation theory.

We can confirm this more directly by projecting the perturbed modes into the basis formed by the unperturbed modes, as shown in Fig. 4f for the lowest-frequency mode

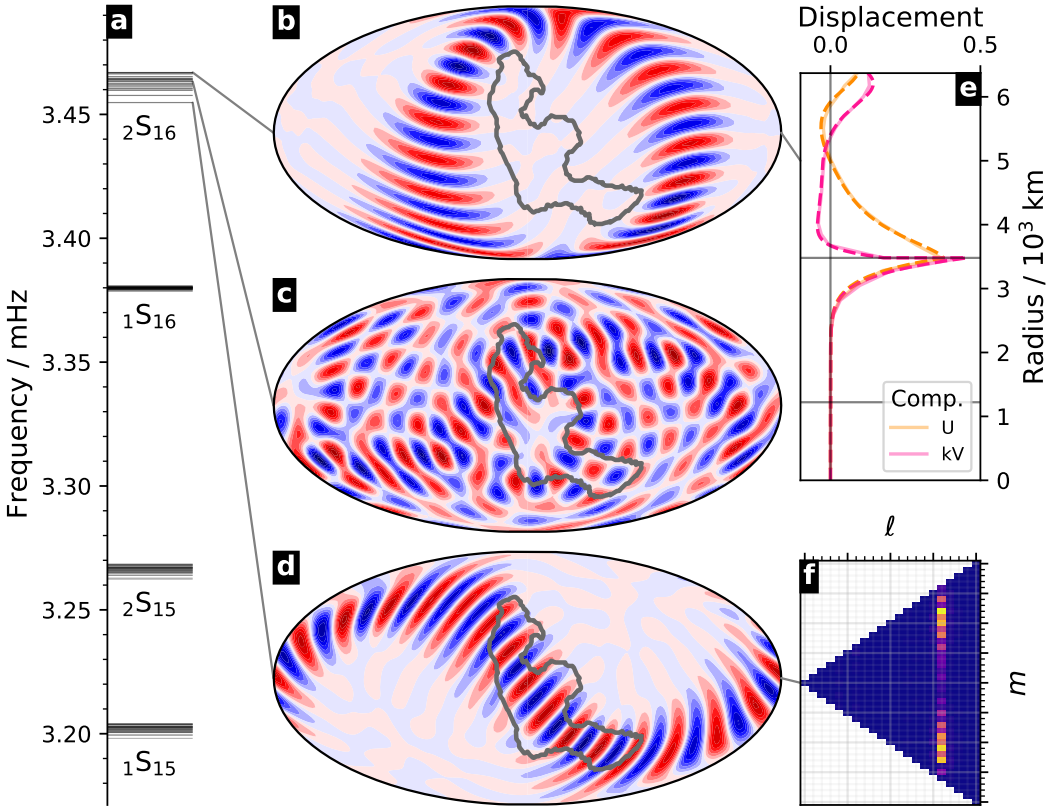

Figure 4. Modes of the first quasi-intersection in an Earth model containing an LLSVP. a) The splitting of the multiplets of the first quasi-intersection (see Fig. 2c) into non-degenerate modes. b, c, d) Radial component of the displacement pattern of three of modes from the $_2S_{16}$ multiplet, as indicated by the gray lines from panel a), sampled at the CMB. The three modes are the highest-, middle-, and lowest-frequency modes of the multiplet. The gray outline shows the edge of the LLSVP. e) The magnitude of the displacement as a function of radius for the mode shown in panel b). Both radial (U) and consoidal (kV) components are shown; the perturbed model also has a small toroidal component, but it is negligible and so it is not shown here. The dashed line shows the profile expected for the unperturbed model; the perturbed and unperturbed lines are almost identical. f) Projection of the displacement of the mode shown in d) into the basis defined by the unperturbed modes. All coefficients are close to zero (blue) except in the $\ell = 16$ band.

of the ${}_2S_{16}$ multiplet. We see the dominant coefficients all come from the same parent multiplet with $n = 2$ and $\ell = 16$. Other small coefficients indicate minor deviation from the isolated multiplet approximation; in other words, coupling with other multiplets (here 'coupling' has the usual mode-seismology meaning). Coupling with other modes is very small, but can be seen with a logarithmic color scale (Supplement S2).

In a more realistic Earth model, the mode coupling, frequency splitting and 'shape' of the modes will also be affected by other lateral heterogeneity and by the planet's rotation. We investigated the effect of rotation (Supplement S3) and find that splitting increases for all modes, but the mixed modes remain markedly more strongly split due to the LLSVP anomaly. The intuitive interpretation of the 'LLSVP-dominated' splitting (Fig. 4) remains valid, but the rotation adds a new group of 'oblateness-dominated' modes.

In summary, these calculations show that mixed modes arise in a realistic Earth model and are unusually sensitive to CMB structures (Fig. 2c and 4e). This sensitivity can be exploited via geographical measurements of the modes' frequency splitting (Fig. 4b,c,d).

4 Discussion

4.1 Previous studies of Stoneley modes

Measurements of splitting of higher-frequency mixed Rayleigh-Stoneley modes are given by Koelemeijer et al. (2013) and Koelemeijer et al. (2015), where they are referred to as Stoneley modes. A systematic search yielded only those modes that were near the first quasi-intersection (the $\ell = 1$ modes ${}_1S_{13}$ to ${}_1S_{16}$, and the $\ell = 2$ modes ${}_2S_{13}$ to ${}_2S_{17}$), the second quasi-intersection (modes ${}_2S_{25}$, ${}_3S_{25}$ and ${}_3S_{26}$), and some lower-frequency Stoneley modes which sample the whole mantle. This can be explained by the mode-mixing phenomenon described here: Stoneley modes far from the branch intersections have no surface (Rayleigh) component, and so are not excitable or observable.

4.2 Perturbation theory

The conventional approach to calculating the modes of a laterally-heterogeneous Earth is to use perturbation theory. We have presented the first calculations of mixed modes using a direct (non-perturbative) approach. The results are qualitatively similar, but in future work we aim to quantify the errors introduced by standard perturbation-theory approaches. These errors may contribute to the misfit of relatively high-frequency

mode data (Deuss & Woodhouse, 2001), especially the effect of CMB topography (Al-Attar et al., 2012), but also lateral heterogeneity and rotation. This may be more important for stronger deviations from spherical symmetry found in other planetary bodies.

4.3 New ways to study Earth's CMB region

Beyond refinement of results from known modes, it may be possible to expand or better constrain the catalog of mixed modes, thanks to new deployments, instrumentation, earthquakes, inverse theory, and signal-processing techniques. In particular, some of the CMB-sensitive modes further from the the quasi-intersections (e.g. modes ${}_2S_{23}$ and ${}_3S_{23}$; see the gallery) might be detectable, perhaps using depth-based stacking (see Lekić et al., 2009), array-based gradiometry (see Schmelzbach et al., 2018), or horizontal-component data (see Schneider & Deuss, 2020), given that Stoneley-mode particle-motion polarization is distinct from that of overlapping Rayleigh modes (compare with Boaga et al., 2013).

We also investigated numerically the possibility of a 'mixed Stoneley-Rayleigh wave' propagating along the parallel waveguides of the outer surface and the CMB, by using mode summation. Our findings are detailed in Supplement S4 and summarized here. For the sum of modes to resemble a traveling wave instead of a standing wave, the mixing must affect enough modes near the intersection. We found that the waveguide coupling is strong enough for an earthquake to generate a Stoneley wave on the CMB, whose wavepacket is quite dispersive, spanning the range of group velocities from the two mode branches. At the Earth's surface, however, the wavefield is dominated by an ordinary Rayleigh wave, with no indication that it is influenced by waveguide coupling. Therefore, although the CMB Stoneley wave is of theoretical interest, we do not expect that mode mixing could be observed in a traveling wave at the surface.

4.4 Modes and waveguide coupling in other settings

Waveguide coupling has been recognized in many non-seismic systems, such as photonic waveguides (Marcuse, 1971; Bertolotti et al., 2017, section 3.4), oceanic gravity waves (Miropol'sky, 2001, section 2.2) and acoustic gravity waves in the atmosphere (Harkrider, 1964). Seismic waveguide coupling is an important example, and we expect it to occur in many settings outside of the solid Earth, such as in ocean basins (Alenitsyn, 1998),

cells with vesicles (Vorselen et al., 2017), solid-state acoustic circuits (see Hess, 2002), floating ice sheets, magma chambers, and planetary bodies containing internal oceans, such as Europa (Anderson et al., 1998) and (perhaps) Pluto (Denton et al., 2020). More generally, the non–perturbation-based approach which we showcase here will allow us study the seismic modes of planets, stars, and asteroids which are far from spherically symmetrical, such as the irregularly-shaped asteroid Apophis.

5 Conclusions

We show that two exponentially-localized seismic waves, propagating along parallel solid-vacuum and solid-fluid interfaces, can couple to form a pair of waves, both of which have a non-zero displacement component near both interfaces. Even if the separation between the two interfaces is large, coupling will occur at frequencies where the two dispersion curves almost intersect. This is an example of the waveguide coupling phenomena found in many branches of physics.

Earth's normal modes also display waveguide coupling. Most dramatically, we show that there is coupling between the free surface and core-mantle boundary, which results in mixed Stoneley-Rayleigh modes. Some of these modes are excitable by earthquakes and are expected to be detectable at the Earth's surface. This clarifies why previous workers have been able to observe higher-frequency Stoneley-like modes, which, in the absence of mode mixing, are exclusively focused at the core-mantle boundary.

We use a new finite-element technique for both spherically-symmetric and laterally-inhomogeneous models to show that mixed-mode frequencies and splitting are unusually sensitive to anomalies in the lower mantle. The concept of mode mixing, and the new tools demonstrated here, may guide future observational studies of mixed Rayleigh-Stoneley modes. Such observations are key to important debates about the lowermost mantle, including the density of LLSVPs and the spatial distribution of post-perovskite. Moreover, mixed modes may be a useful probe for other bodies with strong internal waveguides, for example cells with vesicles, and planetary bodies such as Europa and Pluto. In the coming decades, an abundance of seismic data will be gathered from bodies beyond Earth, which are in many cases far from spherically symmetric. The non–perturbation-based forward modeling demonstrated here will help to understand the interiors of those strange new worlds.

Code availability

The 3-D code, *NormalModes*, is available at `https://github.com/js1019/NormalModes`. The 1-D code, *Ouroboros*, will be made public on GitHub and the FAIR-compliant repository Zenodo at the time of publication. In the meantime, the source code is included as 'Data Set SI - Supplemental Code'. Please do not distribute this code.

Author contribution statement

RDvdH and MVdH conceived the idea of mixed Rayleigh-Stoneley modes. Under the supervision of MVdH: 1. JY carried out semiclassical analysis; 2. JY and JS developed the weak form and implemented a finite-element radial solution; 3. JY first calculated mixed modes; 3. JS implemented a finite-element 3D solution including eigensolver; 4. JH improved the radial code and translated it into Python. Under the supervision of both RDvdH and MVdH: 1. HMD tested semiclassical analysis numerically; 2. HMD calculated modes of 3D LLSVP model; 3. HMD wrote the first draft of paper and prepared figures. RDvdH, MVdH and HMD revised the manuscript, and all authors provided comments on the final draft.

Acknowledgments

MvdH is supported by the Simons Foundation Math + X program, National Science Foundation grant DMS-1815143, and XSEDE allocation EAR170019. HMD is grateful to R. Herrmann, P. Koelemeijer and H. Lau for helpful discussions. For spherical harmonic analysis, we used packages *SHTns* (Schaeffer, 2013) and *SHTools* (Wieczorek & Meschede, 2018). For plotting, we used *Matplotlib* (Hunter, 2007), including *Cartopy* for maps (Met Office, 2015).

References

Al-Attar, D., Woodhouse, J. H., & Deuss, A. (2012, 05). Calculation of normal-mode spectra in laterally heterogeneous Earth models using an iterative direct solution method. *Geophysical Journal International*, *189*(2), 1038-1046. Retrieved from `https://doi.org/10.1111/j.1365-246X.2012.05406.x` doi: 10.1111/j.1365-246X.2012.05406.x

Alenitsyn, A. (1998). Double wave of stoneley type on the interface of a stratified fluid layer and an elastic solid half-space. *The Journal of the Acoustical Soci-*

ety of America, *103*(2), 795-800. Retrieved from https://doi.org/10.1121/1.421242 doi: 10.1121/1.421242

Anderson, J. D., Schubert, G., Jacobson, R. A., Lau, E. L., Moore, W. B., & Sjogren, W. L. (1998). Europa's differentiated internal structure: Inferences from four galileo encounters. *Science*, *281*(5385), 2019–2022. Retrieved from https://science.sciencemag.org/content/281/5385/2019 doi: 10.1126/science.281.5385.2019

Arnold, V. I. (1978). *Mathematical methods of classical mechanics*. Springer-Verlag New York.

Aubert, J., Amit, H., Hulot, G., & Olson, P. (2008, 8 01). Thermochemical flows couple the earth's inner core growth to mantle heterogeneity. *Nature*, *454*(7205), 758-761. Retrieved from https://doi.org/10.1038/nature07109 doi: 10.1038/nature07109

Bertolotti, M., Sibilia, C., & Guzman, A. M. (2017). *Evanescent waveguides in optics*. Springer. doi: 10.1007/978-3-319-61261-4

Biswas, N. N. (1972, 12 01). Earth-flattening procedure for the propagation of rayleigh wave. *Pure and Applied Geophysics*, *96*(1), 61-74. Retrieved from https://doi.org/10.1007/BF00875629 doi: 10.1007/BF00875629

Biswas, N. N., & Knopoff, L. (1970, 08). Exact earth-flattening calculation for Love waves. *Bulletin of the Seismological Society of America*, *60*(4), 1123-1137. Retrieved from https://pubs.geoscienceworld.org/ssa/bssa/article-abstract/60/4/1123/116804/

Boaga, J., Cassiani, G., Strobbia, C. L., & Vignoli, G. (2013). Mode misidentification in rayleigh waves: Ellipticity as a cause and a cure. *GEOPHYSICS*, *78*(4), EN17-EN28. Retrieved from https://doi.org/10.1190/geo2012-0194.1 doi: 10.1190/geo2012-0194.1

Buffett, B. A. (2002). Estimates of heat flow in the deep mantle based on the power requirements for the geodynamo. *Geophysical Research Letters*, *29*(12). Retrieved from https://agupubs.onlinelibrary.wiley.com/doi/abs/10.1029/2001GL014649 doi: 10.1029/2001GL014649

Chapman, C. H. (1973). The earth-flattening transformation in body-wave theory. *Geophysical Journal of the Royal Astronomical Society*, *35*(1-3), 55-70. Retrieved from https://onlinelibrary.wiley.com/doi/abs/10.1111/

j.1365-246X.1973.tb02414.x doi: 10.1111/j.1365-246X.1973.tb02414.x

Cottaar, S., & Lekić, V. (2016, 08). Morphology of seismically slow lower-mantle structures. *Geophysical Journal International*, *207*(2), 1122-1136. Retrieved from https://dx.doi.org/10.1093/gji/ggw324 doi: 10.1093/gji/ggw324

Dahlen, F. A., & Tromp, J. (1998). *Theoretical global seismology.* Princeton University Press.

Denton, C. A., Johnson, B. C., Freed, A. M., & Melosh, H. J. (2020, 3). *Seismology on pluto?! antipodal terrains produced by sputnik planitia-forming impact.* Retrieved from https://www.hou.usra.edu/meetings/lpsc2020/pdf/1220.pdf (51st Lunar and Planetary Science Conference, Texas)

Deuss, A., & Woodhouse, J. H. (2001, 09). Theoretical free-oscillation spectra: The importance of wide band coupling. *Geophysical Journal International*, *146*(3), 833-842. Retrieved from https://doi.org/10.1046/j.1365-246X.2001.00502.x doi: 10.1046/j.1365-246X.2001.00502.x

Dziewonski, A. M., & Anderson, D. L. (1981). Preliminary reference earth model. *Physics of the Earth and Planetary Interiors*, *25*(4), 297 - 356. Retrieved from http://www.sciencedirect.com/science/article/pii/0031920181900467 doi: 10.1016/0031-9201(81)90046-7

Harkrider, D. G. (1964). Theoretical and observed acoustic-gravity waves from explosive sources in the atmosphere. *Journal of Geophysical Research (1896-1977)*, *69*(24), 5295-5321. Retrieved from https://agupubs.onlinelibrary.wiley.com/doi/abs/10.1029/JZ069i024p05295 doi: 10.1029/JZ069i024p05295

Haskell, N. A. (1964, 02). Radiation pattern of surface waves from point sources in a multi-layered medium. *Bulletin of the Seismological Society of America*, *54*(1), 377-393. Retrieved from https://pubs.geoscienceworld.org/ssa/bssa/article-abstract/54/1/377/101441/

Herrmann, R. B. (2013). Computer Programs in Seismology: An evolving tool for instruction and research. *Seismological Research Letters*, *84*(6), 1081. Retrieved from http://dx.doi.org/10.1785/0220110096 doi: 10.1785/0220110096

Hess, P. (2002). Surface acoustic waves in materials science. *Physics Today*, *55*(3), 42-47. Retrieved from https://doi.org/10.1063/1.1472393 doi: 10.1063/1

.1472393

Hirose, K., Labrosse, S., & Hernlund, J. (2013). Composition and state of the core. *Annual Review of Earth and Planetary Sciences*, *41*(1), 657-691. Retrieved from https://doi.org/10.1146/annurev-earth-050212-124007 doi: 10.1146/annurev-earth-050212-124007

Hunter, J. D. (2007). Matplotlib: A 2d graphics environment. *Computing In Science & Engineering*, *9*(3), 90–95. doi: 10.1109/MCSE.2007.55

Irving, J. C. E., Cottaar, S., & Lekić, V. (2018). Seismically determined elastic parameters for earth's outer core. *Science Advances*, *4*(6). Retrieved from https://advances.sciencemag.org/content/4/6/eaar2538 doi: 10.1126/sciadv.aar2538

Ishii, M., & Tromp, J. (1999). Normal-mode and free–air-gravity constraints on lateral variations in velocity and density of earth's mantle. *Science*, *285*(5431), 1231–1236. Retrieved from http://science.sciencemag.org/content/285/5431/1231 doi: 10.1126/science.285.5431.1231

Kellogg, L. H., Hager, B. H., & van der Hilst, R. D. (1999). Compositional stratification in the deep mantle. *Science*, *283*(5409), 1881–1884. Retrieved from https://science.sciencemag.org/content/283/5409/1881 doi: 10.1126/science.283.5409.1881

Kennett, B. L. N. (1998, 02). On the density distribution within the Earth. *Geophysical Journal International*, *132*(2), 374-382. Retrieved from https://doi.org/10.1046/j.1365-246x.1998.00451.x doi: 10.1046/j.1365-246x.1998.00451.x

Koelemeijer, P., Deuss, A., & Ritsema, J. (2013). Observations of core–mantle-boundary stoneley modes. *Geophysical Research Letters*, *40*(11), 2557-2561. Retrieved from https://agupubs.onlinelibrary.wiley.com/doi/abs/10.1002/grl.50514 doi: 10.1002/grl.50514

Koelemeijer, P., Deuss, A., & Ritsema, J. (2017, 05 15). Density structure of earth's lowermost mantle from stoneley-mode splitting observations. *Nature Communications*, *8*(1), 15241. Retrieved from https://doi.org/10.1038/ncomms15241 doi: 10.1038/ncomms15241

Koelemeijer, P., Ritsema, J., Deuss, A., & van Heijst, H.-J. (2015, 12). SP12RTS: a degree-12 model of shear- and compressional-wave velocity for Earth's man-

tle. *Geophysical Journal International*, *204*(2), 1024-1039. Retrieved from https://doi.org/10.1093/gji/ggv481 doi: 10.1093/gji/ggv481

Koelemeijer, P., Schuberth, B., Davies, D., Deuss, A., & Ritsema, J. (2018). Constraints on the presence of post-perovskite in earth's lowermost mantle from tomographic-geodynamic model comparisons. *Earth and Planetary Science Letters*, *494*, 226 - 238. Retrieved from http://www.sciencedirect.com/science/article/pii/S0012821X18302656 doi: 10.1016/j.epsl.2018.04.056

Komatitsch, D., & Tromp, J. (2002). Spectral-element simulations of global seismic wave propagation—i. validation. *Geophysical Journal International*, *149*(2), 390-412. Retrieved from https://onlinelibrary.wiley.com/doi/abs/10.1046/j.1365-246X.2002.01653.x doi: https://doi.org/10.1046/j.1365-246X.2002.01653.x

Lau, H. C. P., Faul, U., Mitrovica, J. X., Al-Attar, D., Tromp, J., & Garapić, G. (2016, 10). Anelasticity across seismic to tidal timescales: a self-consistent approach. *Geophysical Journal International*, *208*(1), 368-384. Retrieved from https://doi.org/10.1093/gji/ggw401 doi: 10.1093/gji/ggw401

Lau, H. C. P., Mitrovica, J. X., Davis, J. L., Tromp, J., Yang, H.-Y., & Al-Attar, D. (2017, 11 01). Tidal tomography constrains earth's deep-mantle buoyancy. *Nature*, *551*(7680), 321-326. Retrieved from https://doi.org/10.1038/nature24452 doi: 10.1038/nature24452

Lay, T. (2015). 1.22 - deep earth structure: Lower mantle and d". In G. Schubert (Ed.), *Treatise on geophysics (second edition)* (Second Edition ed., p. 683 - 723). Oxford: Elsevier. Retrieved from http://www.sciencedirect.com/science/article/pii/B9780444538024000191 doi: 10.1016/B978-0-444-53802-4.00019-1

Lay, T., Hernlund, J., & Buffett, B. A. (2008, 1 01). Core–mantle-boundary heat flow. *Nature Geoscience*, *1*(1), 25-32. Retrieved from https://doi.org/10.1038/ngeo.2007.44 doi: 10.1038/ngeo.2007.44

Lekić, V., Matas, J., Panning, M., & Romanowicz, B. (2009). Measurement and implications of frequency dependence of attenuation. *Earth and Planetary Science Letters*, *282*(1), 285 - 293. Retrieved from http://www.sciencedirect.com/science/article/pii/S0012821X09001800 doi: https://doi.org/10.1016/j.epsl.2009.03.030

Marcuse, D. (1971). The coupling of degenerate modes in two parallel dielectric waveguides. *The Bell System Technical Journal*, *50*(6), 1791-1816. Retrieved from https://ieeexplore.ieee.org/document/6771781 doi: 10.1002/j.1538-7305.1971.tb02582.x

Masters, G., Woodhouse, J. H., & Freeman, G. (2011). *Mineos.* Retrieved from https://geodynamics.org/cig/software/mineos/

Met Office. (2015). Cartopy: a cartographic Python library with a Matplotlib interface [Computer software manual]. Exeter, Devon. Retrieved from http://scitools.org.uk/cartopy

Miropol'sky, Y. Z. (2001). *Dynamics of internal gravity waves in the ocean.* Springer. doi: 10.1007/978-94-017-1325-2

Mosca, I., Cobden, L., Deuss, A., Ritsema, J., & Trampert, J. (2012). Seismic and mineralogical structures of the lower mantle from probabilistic tomography. *Journal of Geophysical Research: Solid Earth*, *117*(B6). Retrieved from https://agupubs.onlinelibrary.wiley.com/doi/abs/10.1029/2011JB008851 doi: 10.1029/2011JB008851

Moulik, P., & Ekström, G. (2016). The relationships between large-scale variations in shear velocity, density, and compressional velocity in the earth's mantle. *Journal of Geophysical Research: Solid Earth*, *121*(4), 2737-2771. Retrieved from https://agupubs.onlinelibrary.wiley.com/doi/abs/10.1002/2015JB012679 doi: 10.1002/2015JB012679

Resovsky, J. S., & Ritzwoller, M. H. (1999). Regularization uncertainty in density models estimated from normal-mode data. *Geophysical Research Letters*, *26*(15), 2319-2322. Retrieved from https://agupubs.onlinelibrary.wiley.com/doi/abs/10.1029/1999GL900540 doi: 10.1029/1999GL900540

Romanowicz, B. (2001). Can we resolve 3d density heterogeneity in the lower mantle? *Geophysical Research Letters*, *28*(6), 1107-1110. Retrieved from https://agupubs.onlinelibrary.wiley.com/doi/abs/10.1029/2000GL012278 doi: 10.1029/2000GL012278

Schaeffer, N. (2013, Mar). Efficient spherical harmonic transforms aimed at pseudospectral numerical simulations. *Geochemistry, Geophysics, Geosystems*, *14*(3), 751–758. Retrieved from http://dx.doi.org/10.1002/ggge.20071 doi: 10.1002/ggge.20071

Schmelzbach, C., Donner, S., Igel, H., Sollberger, D., Taufiqurrahman, T., Bernauer, F., ... Robertsson, J. (2018). Advances in 6c seismology: Applications of combined translational and rotational motion measurements in global and exploration seismology. *Geophysics*, *83*(3), WC53-WC69. Retrieved from https://doi.org/10.1190/geo2017-0492.1 doi: 10.1190/geo2017-0492.1

Schneider, S., & Deuss, A. (2020, 11). A new catalogue of toroidal-mode overtone splitting function measurements. *Geophysical Journal International*, *225*(1), 329-341. Retrieved from https://doi.org/10.1093/gji/ggaa567 doi: 10.1093/gji/ggaa567

Scholte, J. G. (1942). On the stoneley-wave equation. *Proceedings of the Koninklijke Nederlandse Akademie van Wetenschappen*, *45*, 20-25. Retrieved from https://www.dwc.knaw.nl/DL/publications/PU00017694.pdf

Shi, J., Li, R., Xi, Y., Saad, Y., & de Hoop, M. V. (2018). Computing planetary interior normal modes with a highly-parallel polynomial-filtering eigensolver. In *Proceedings of the international conference for high performance computing, networking, storage, and analysis* (pp. 71:1–71:13). Piscataway, NJ, USA: IEEE Press. Retrieved from https://doi.org/10.1109/SC.2018.00074 doi: 10.1109/SC.2018.00074

Shi, J., Li, R., Xi, Y., Saad, Y., & de Hoop, M. V. (2019). *A rayleigh–ritz-method-based approach to computing seismic normal modes in rotating terrestrial planets.* Retrieved from https://arxiv.org/abs/1906.11082

Stoneley, R. (1924). Elastic waves at the surface of separation of two solids. *Proceedings of the Royal Society of London A*, *106*, 416–428. doi: 10.1098/rspa.1924.0079

Strutt, J. W. (1885). On waves propagated along the plane surface of an elastic solid. *Proceedings of the London Mathematical Society*, *s1-17*(1), 4-11. Retrieved from https://londmathsoc.onlinelibrary.wiley.com/doi/abs/10.1112/plms/s1-17.1.4 doi: 10.1112/plms/s1-17.1.4

Tackley, P. J. (2012). Dynamics and evolution of the deep mantle resulting from thermal, chemical, phase and melting effects. *Earth-Science Reviews*, *110*(1), 1 - 25. Retrieved from http://www.sciencedirect.com/science/article/pii/S0012825211001486 doi: 10.1016/j.earscirev.2011.10.001

Tkalčić, H., & Romanowicz, B. (2002). Short-scale heterogeneity in the lowermost

mantle: insights from pcp-p and scs-s data. *Earth and Planetary Science Letters*, *201*(1), 57 - 68. Retrieved from http://www.sciencedirect.com/science/article/pii/S0012821X0200657X doi: 10.1016/S0012-821X(02)00657-X

Trampert, J., Deschamps, F., Resovsky, J., & Yuen, D. (2004). Probabilistic tomography maps chemical heterogeneities throughout the lower mantle. *Science*, *306*(5697), 853–856. Retrieved from https://science.sciencemag.org/content/306/5697/853 doi: 10.1126/science.1101996

Vorselen, D., MacKintosh, F. C., Roos, W. H., & Wuite, G. J. (2017, 3 28). Competition between bending and internal pressure governs the mechanics of fluid nanovesicles. *ACS Nano*, *11*(3), 2628-2636. Retrieved from https://doi.org/10.1021/acsnano.6b07302 doi: 10.1021/acsnano.6b07302

Wang, C. Y., & Herrmann, R. B. (1980, 08). A numerical study of P-, SV-, and SH-wave generation in a plane layered medium. *Bulletin of the Seismological Society of America*, *70*(4), 1015-1036.

Wang, Y., & Wen, L. (2007). Geometry and p- and s-velocity structure of the "african anomaly". *Journal of Geophysical Research: Solid Earth*, *112*(B5). Retrieved from https://agupubs.onlinelibrary.wiley.com/doi/abs/10.1029/2006JB004483 doi: 10.1029/2006JB004483

Wieczorek, M. A., & Meschede, M. (2018). Shtools: Tools for working with spherical harmonics. *Geochemistry, Geophysics, Geosystems*, *19*(8), 2574-2592. Retrieved from https://agupubs.onlinelibrary.wiley.com/doi/abs/10.1029/2018GC007529 doi: 10.1029/2018GC007529

Woodhouse, J. H. (1978). Asymptotic results for elastodynamic propagator matrices in plane-stratified and spherically-stratified earth models. *Geophysical Journal of the Royal Astronomical Society*, *54*(2), 263-280. Retrieved from https://onlinelibrary.wiley.com/doi/abs/10.1111/j.1365-246X.1978.tb04259.x doi: 10.1111/j.1365-246X.1978.tb04259.x

Ye, J. (2018). *Revisiting the computation of normal modes in snrei models of planets - close eigenfrequencies* (Master's thesis, Rice University). Retrieved from https://hdl.handle.net/1911/104942

Zhang, N., & Zhong, S. (2011). Heat fluxes at the earth's surface and core-mantle boundary since pangea formation and their implications for the geomag-

netic superchrons. *Earth and Planetary Science Letters*, *306*(3), 205 - 216. Retrieved from http://www.sciencedirect.com/science/article/pii/S0012821X11002068 doi: 10.1016/j.epsl.2011.04.001

Zhao, L., & Dahlen, F. A. (1993, 12). Asymptotic eigenfrequencies of the Earth's normal modes. *Geophysical Journal International*, *115*(3), 729-758. Retrieved from https://doi.org/10.1111/j.1365-246X.1993.tb01490.x doi: 10.1111/j.1365-246X.1993.tb01490.x

Supporting information for

Mixed Mixed Rayleigh-Stoneley modes: Analysis of seismic waveguide coupling and sensitivity to lower-mantle structures

Harry Matchette-Downes[*,1], Jia Shi[2,a], Jingchen Ye[3,4,b], Jiayuan Han[2], Robert D. van der Hilst[1], and Maarten V. de Hoop[2,3]

[*]Corresponding author: hrmd@mit.edu

[1]Department of Earth, Atmospheric and Planetary Sciences, Massachusetts Institute of Technology, 77 Massachusetts Avenue, MA 02139, U.S.A.

[2]Department of Earth, Environmental and Planetary Sciences, Rice University, 6100 Main Street, TX 77005, U.S.A.

[3]Department of Computational and Applied Mathematics, Rice University, 6100 Main Street, TX 77005, U.S.A.

[4]Applied Physics Program, Rice University, 6100 Main Street, TX 77005, U.S.A.

[a]Now at: Shell International Exploration and Production Inc.

[b]Now at: Google LLC.

Contents of this file

- Supplement S1: Group velocity.
- Supplement S2: Projection into unperturbed basis.
- Supplement S3: Effects of rotation.
- Supplement S4: Traveling-wave behavior.
- Supplement S5: Mode gallery.

S1 Group velocity

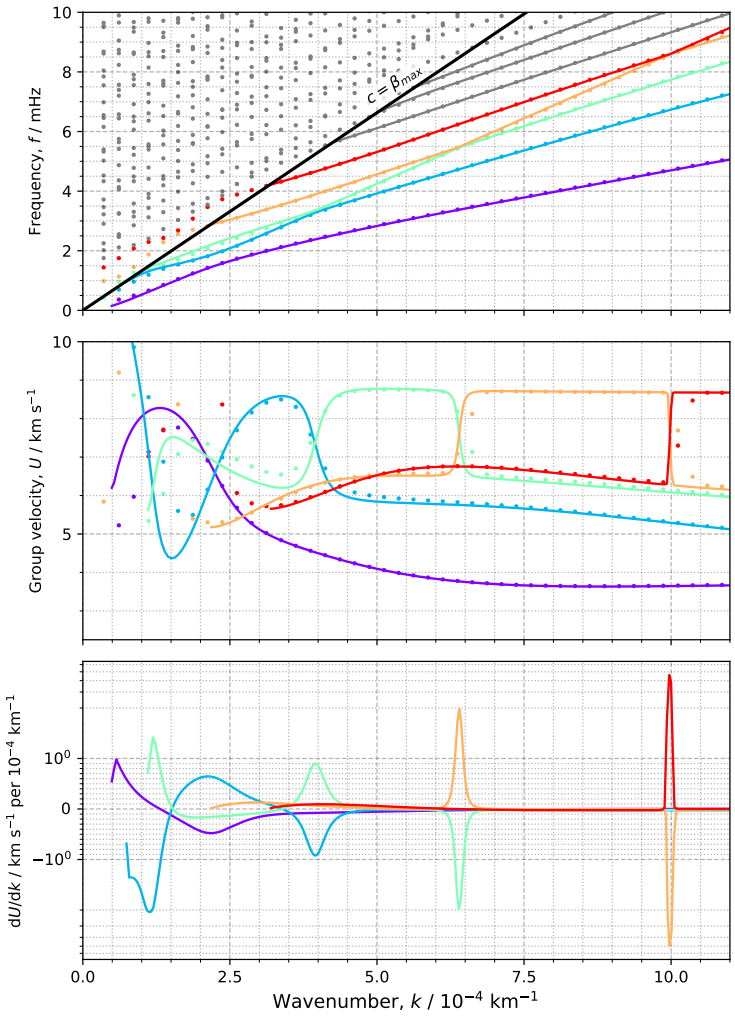

Figure S1: a) Dispersion diagram for modes, shown as points, and the half-space approximation, shown as solid lines. b) Group velocity, calculated from the dispersion diagram, for the first five branches. c) The (continuous) first derivative of the group velocity, illustrating that the group velocity is a smooth function of wavenumber. Note the change from a linear y-axis (between -1 and 1) to a logarithmic one.

S2 Projection of perturbed modes into basis of unperturbed modes

The modes of the spherically-symmetric reference model form a complete basis within the sphere. The perturbed modes can be projected into this basis, as shown here (Supp. Fig. S2) for the lowest-frequency mode of the ${}_2\mathrm{S}_{16}$ multiplet (see Fig. 4d,f in the main text). The basis functions are normalized using the *Mineos* normalization.

The unperturbed mode basis is used in the perturbation-theory approach to calculate the modes and frequencies of the perturbed model. A common assumption in this approach is the 'isolated multiplet' approximation, where the modes of a perturbed multiplet are calculated using only the modes of the same multiplet, before perturbation, as the basis. The coefficients in Supp. Fig. S2 are mostly close to zero, except for the ${}_2\mathrm{S}_{16}^m$ coefficients, indicating that the isolated multiplet approximation is a good approximation. However, we can also see weak coupling with ${}_2\mathrm{S}_{15}$, ${}_2\mathrm{S}_{17}$, ${}_1\mathrm{S}_{15}$, ${}_1\mathrm{S}_{16}$, ${}_1\mathrm{S}_{17}$, ${}_6\mathrm{S}_6$ and ${}_3\mathrm{T}_5$.

The power spectrum of the LLSVP anomaly used in our calculation is shown in Supp. Fig. S3. It is dominated by the $\ell = 1$ band.

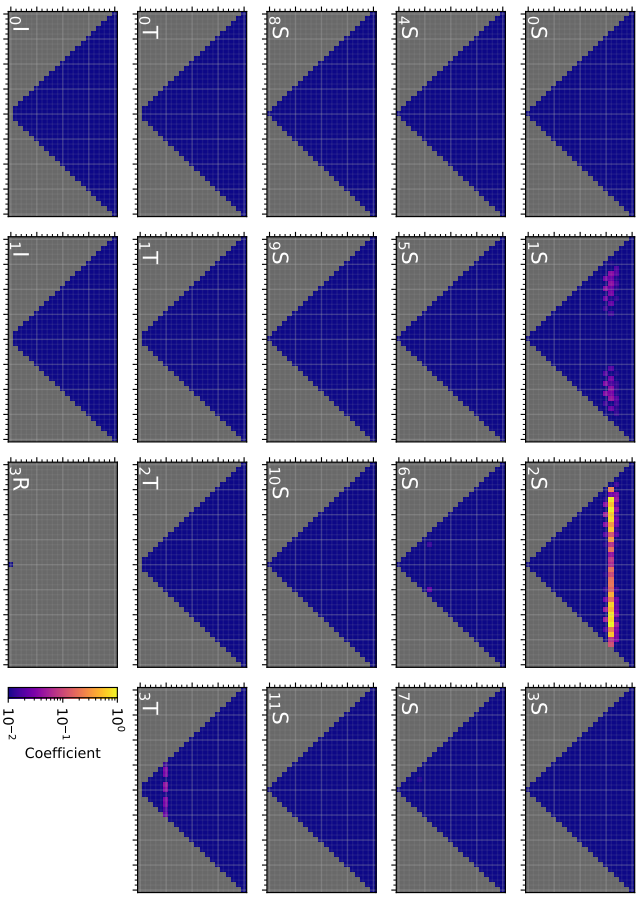

Figure S2: Projection of one of the perturbed modes from the ${}_2\mathrm{S}_{16}$ multiplet into the unperturbed-mode basis. Each panel shows the coefficients $C_{l,m}$ for a given mode branch ${}_nX$. Only branches with modes within 0.5 mHz of the the target mode are shown. For each panel, the x-axis corresponds to the angular degree m and the y-axis corresponds to angular order ℓ.

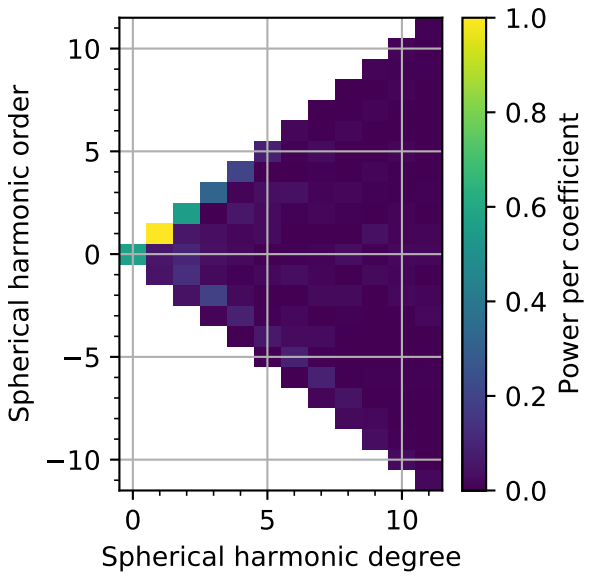

Figure S3: The spherical harmonic power spectrum of the LLSVP anomaly (shown in outline in Fig. 4b,c,d). The power is normalized to the largest coefficient.

S3 Effect of Earth's rotation on the mixed modes

We can make the 3-D mode calculations from the main text (section 3.3) more realistic by including the effects of Earth's rotation: oblateness, centripetal potential, and Coriolis force. Our approach is described in Shi et al. (in review). We assume a rotation period of 23.9345 hours, and calculate the ellipticity as a function of radius using Radau's approximation to Clairault's equation (Dahlen and Tromp, 1998, equation 14.20). Once rotation is including, the eigenfunction vector fields become complex, representing eastward- or westward-propagating waves. The frequencies and spatial displacement patterns are also altered, as we discuss below.

We first note that rotation increases the 'splitting' of each multiplet (which we define as difference between the highest and lowest singlets within a given multiplet). This can be seen by comparing the splitting in the rotating case (Supp. Fig. S4) with the non-rotating case (Fig. 1c); note the change in marker scaling. Although all modes have greater splitting, the splitting of the mixed modes is still markedly stronger due to their sensitivity to the LLSVP anomaly. As an aside, we note that all of the multiplets have a positive shift in their center frequency (the mean of the singlet frequencies).

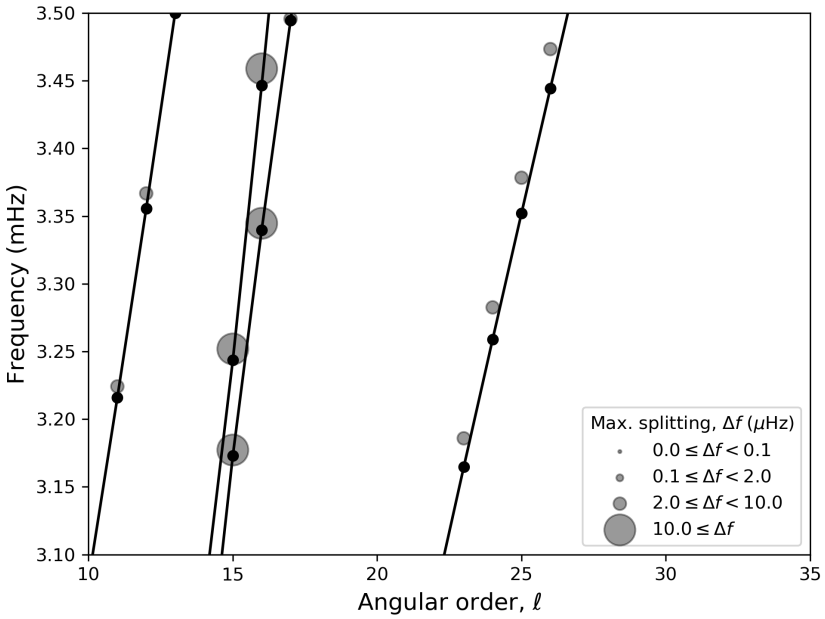

Figure S4: Frequency splitting of each degenerate multiplet in a model with rotation and an LLSVP anomaly. The modes of the spherically-symmetrical reference model are shown as solid lines with opaque dots.

This additional splitting can be understood by examining the eigenfunctions, for example for the mode ${}_1S_{15}$ in Supp. Fig. S5. As we saw in the non-rotating case (Fig. 4), a range of frequencies arises from modes concentrated inside or outside the LLSVP ('LLSVP-dominated'). This range is augmented by a group of modes whose shape is controlled primarily by Earth's oblate shape ('oblateness-dominated'). These modes have wider, more regular frequency separation, with lower-frequency modes being more concentrated at the equator. Note that the number of singlets does not change.

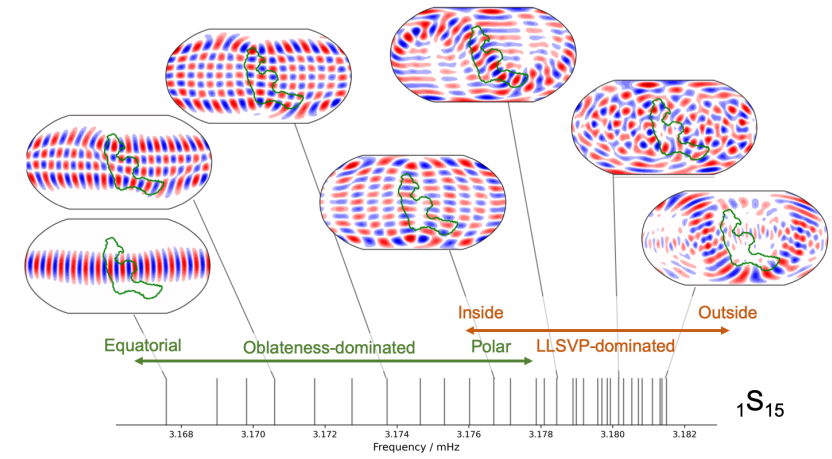

Figure S5: Selected eigenfunctions for multiplet $_1S_{15}$, showing relationship to frequency splitting. Each map shows the real part of the vertical-component displacement field at Earth's surface for a given mode.

This behavior is found in all of the mixed modes and most of the other modes which we calculated (not shown here). A complicating factor is mode coupling, which becomes stronger when rotation is included. We do not discuss mode coupling in detail here, although in future we plan to compare the mode coupling in the direct 3-D approach to the predictions of perturbation theory.

S4 Illustration of traveling-wave behavior

It is well-known that summation of normal modes along a branch yields a traveling wave. We investigated whether summation of the modes of the second quasi-intersection produces any unusual traveling-wave behavior. The modes used in the summation are shown in Supp. Fig. S6. Each mode marker is scaled according to the globally-averaged RMS excitation of that mode, given our choice of source, which was the point CMT approximation of the 2011 Tohoku earthquake. Note that these calculations were carried out in *Mineos* and include the effect of attenuation, unlike other mode calculations in this paper.

We restricted the summation to modes from the two intersecting branches ($n = 2$ and $n = 3$) within a narrow frequency band indicated by the outer pair of gray horizontal lines. A cosine frequency taper was applied to this band, so that modes outside the inner pair of gray horizontal lines had reduced amplitude. It can be seen that the Stoneley branch has low excitation amplitudes, typically around 100 times weaker than the Rayleigh branch.

The contributions of the two branches can be visualized in Supp. Fig. S7. From the left column, we see that the Rayleigh branch resembles a traveling wave in the middle and upper mantle, but in the lower mantle it resembles a standing wave, due to contributions from just a small number of mixed modes at these depths. The middle column shows that the Stoneley branch resembles a standing wave throughout the planet, because only a few modes are excited. The net effect, shown in the right column, appears to have a traveling wave in the upper mantle and on the CMB.

We can understand the results of the full summation by plotting the velocity field as a seismic section with increasing distance from the source (Supp. Fig. S8). The plot also shows the group velocities of the modes (calculated using *Mineos*) for a selection of modes. The wavefield at the surface is a traveling wave whose group velocity is well described by the 'normal' Rayleigh modes before and after the quasi-intersection region (e.g. modes ${}_3S_{22}$ and ${}_2S_{28}$). In other words, the surface wavefield is dominated by the second Rayleigh overtone.

By contrast, if we plot the wavefield just above the core-mantle boundary (Supp. Fig. S9), a different traveling wave arises. This wavepacket is more dispersive, with group velocities ranging between the Rayleigh and Stoneley group velocities found further from the intersection. Note that the amplitude of this wave is around 10 times smaller than the surface wave.

We interpret this CMB wave in the following way: near the quasi-intersection, the Rayleigh modes have a small Stoneley component at the CMB, and the Stoneley modes have a small Rayleigh component at the surface. When carrying out the normal-mode summation near the quasi-intersection, if all of these modes are included, the excitation amplitudes are large enough over a sufficiently wide bandwidth to produce a traveling wave on the CMB. The wavepacket is broad due to the wide range of group velocities of the contributing modes. We call this a 'mixed Stoneley-Rayleigh wave'

Unfortunately, if a corresponding 'mixed Rayleigh-Stoneley wave' exists and propagates along the free surface, its amplitude must be very small as it is not visible in Supp. Fig. S8. Therefore, although it is interesting to know about the CMB wave, it is not of practical use.

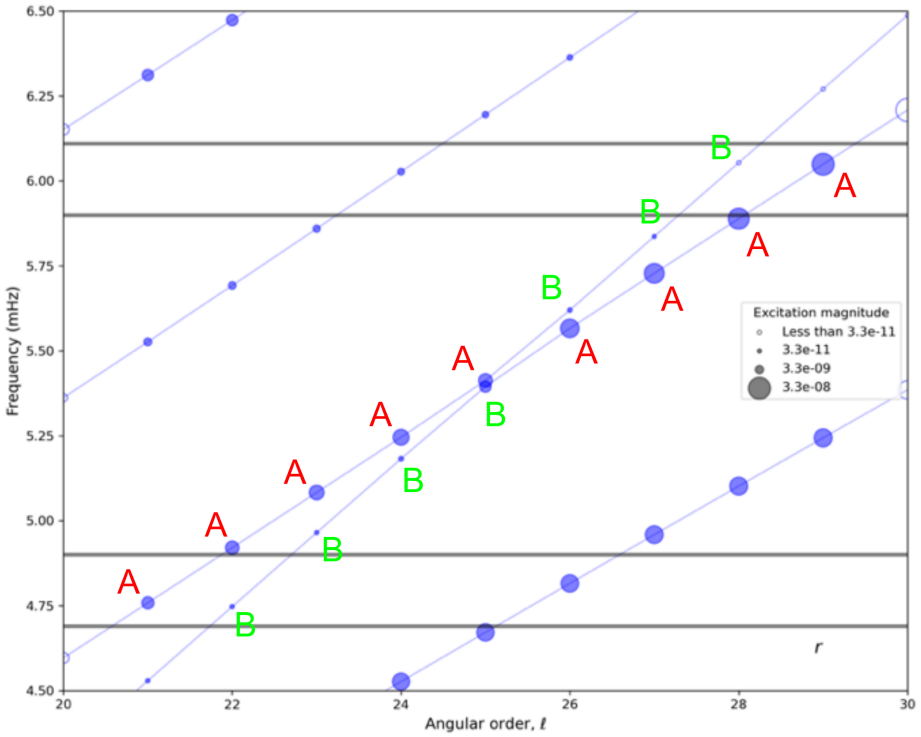

Figure S6: Mode diagram showing detail of the second quasi-intersection. Marker symbols are scaled by the excitation of each mode (in S.I. units). Second-overtone Rayleigh modes are labeled 'A', and Stoneley modes are labeled 'B' (although this distinction is arbitrary in the case of the mixed modes).

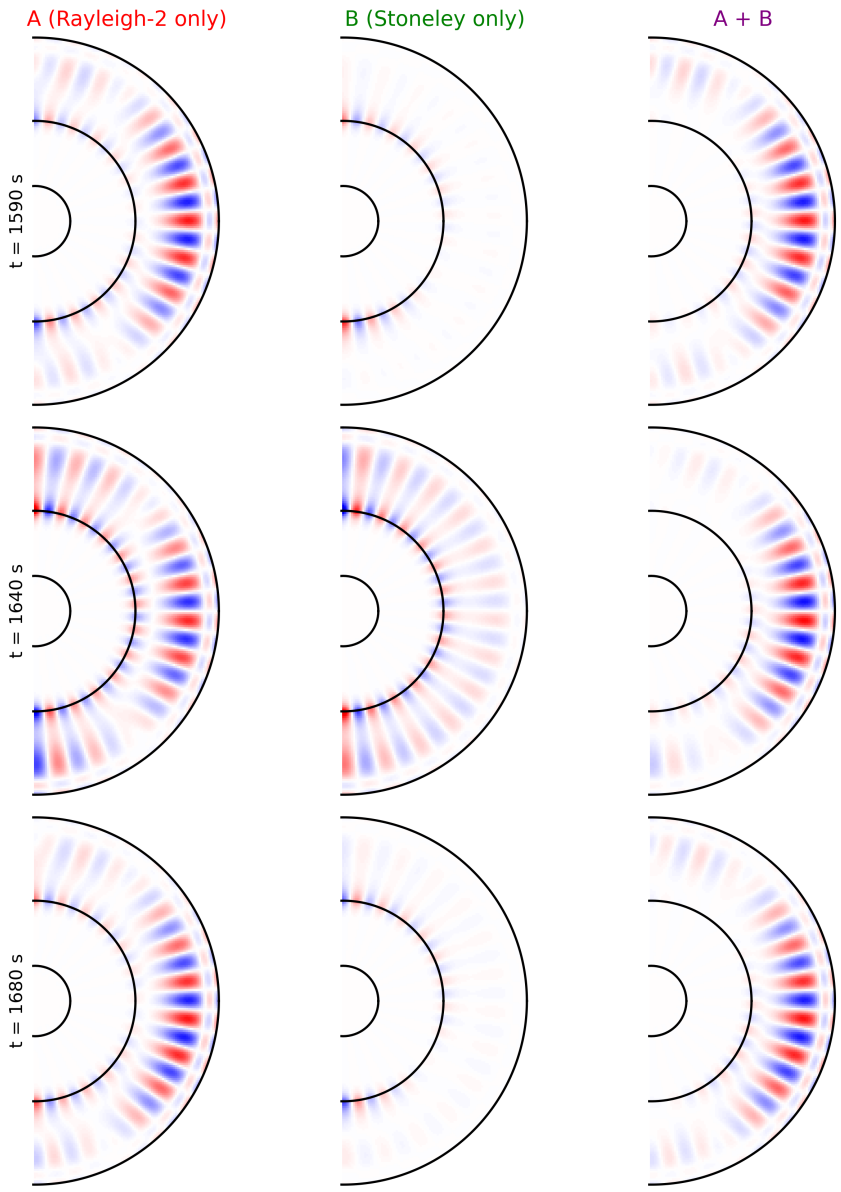

Figure S7: Plots of the vertical velocity field at various times (indicated on the left-hand side) after the earthquake, decomposed into contributions from different mode branches (indicated at the top). The color scale is the same for each panel. The source location is at the top of each panel.

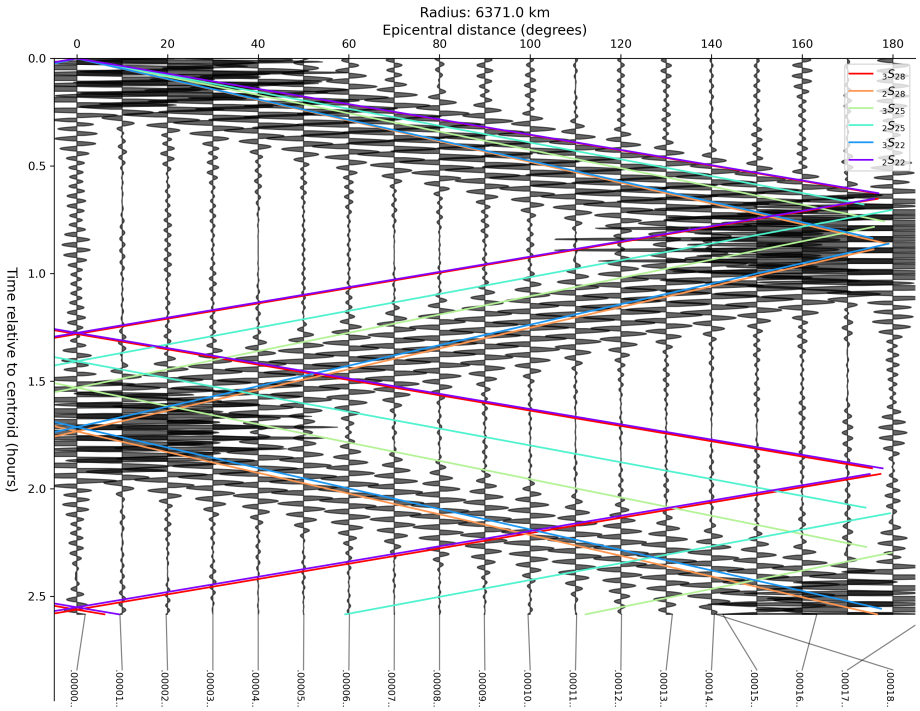

Figure S8: Seismic section observed at the surface. Each trace shows the particle velocity at the specified epicentral distance. Traces are normalized by a common value so that relative amplitudes are preserved. Mode group velocities are indicated by colored lines as shown in the legend.

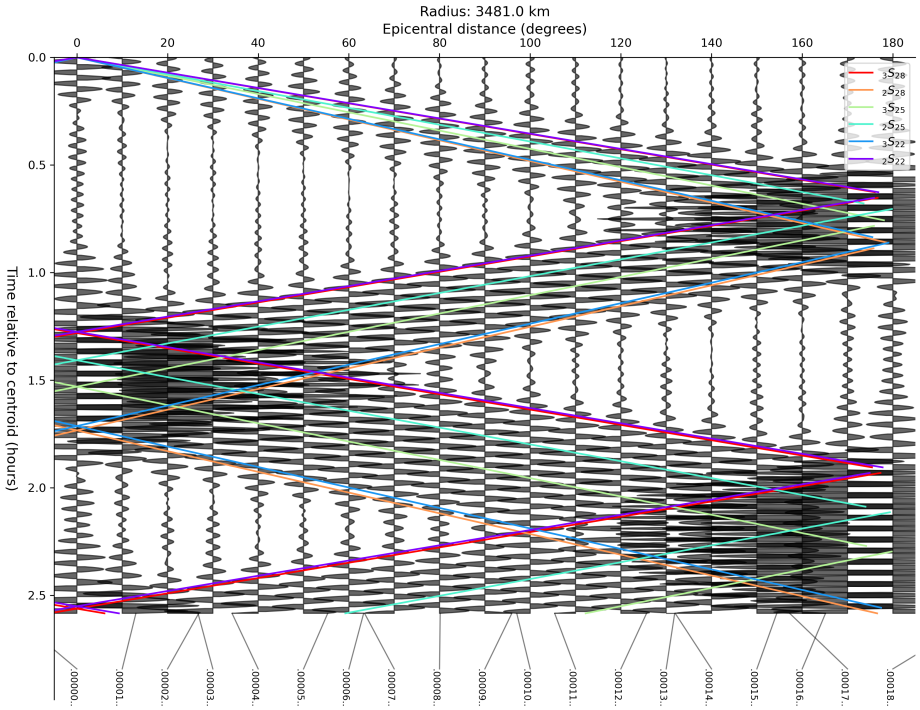

Figure S9: The same as Supp. Fig. S8, except the particle velocity is plotted at the CMB instead of the surface.

S5 Gallery of modes near quasi-intersections

Here we show the eigenfunctions for modes in the vicinity of the first, second and third quasi-intersections, calculated using the *Mineos* code. In contrast with the main text, we include the effects of attenuation and the perturbation to the gravitational potential, to make these calculations as realistic as possible. Nonetheless, given that mode mixing is sensitive to small shifts in mode frequencies, this gallery should not be used to pin-point mode-mixing frequencies on the real Earth, because we have neglected the effects of anisotropy, rotation, and three-dimensional structures, including ellipticity and the crust and ocean.

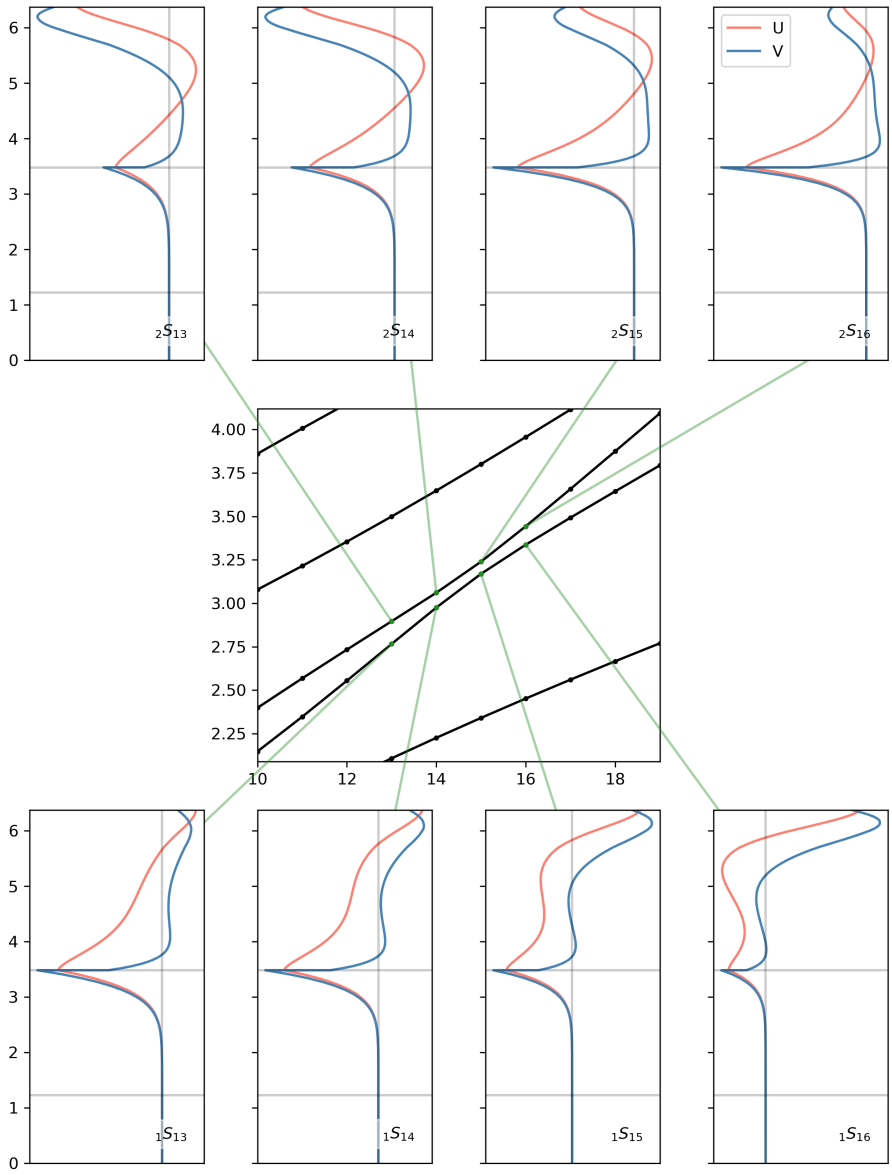

Figure S10: Summary of eigenfunctions of modes near the first quasi-intersection. The central panel shows the location of the modes on the dispersion diagram (ℓ versus frequency in mHz). For each mode, the radial and consoidal components are shown, including the factor of k omitted in some conventions. The y-axis shows radial coordinate in units of 10^3 km and horizontal lines indicate the CMB and ICB discontinuities.

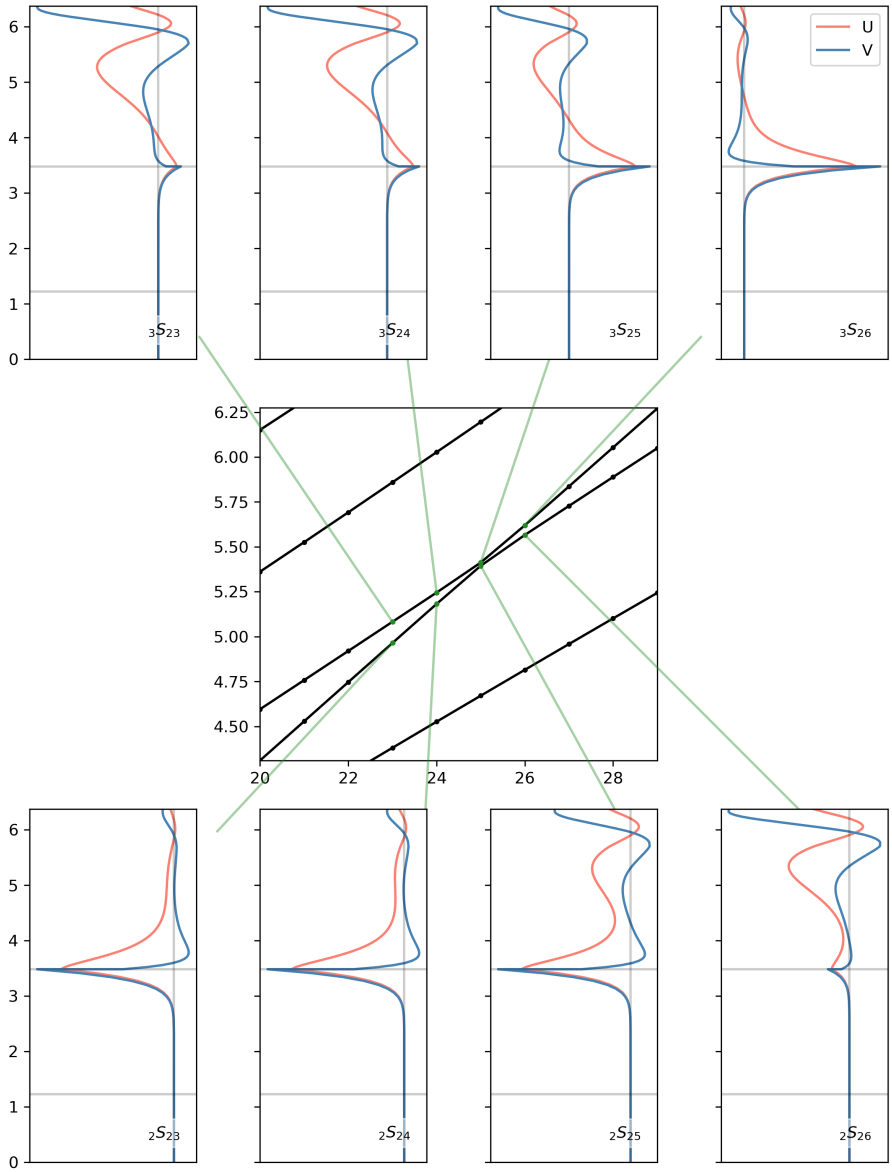

Figure S11: Same as Supp. Fig. S10, but for the second quasi-intersection.

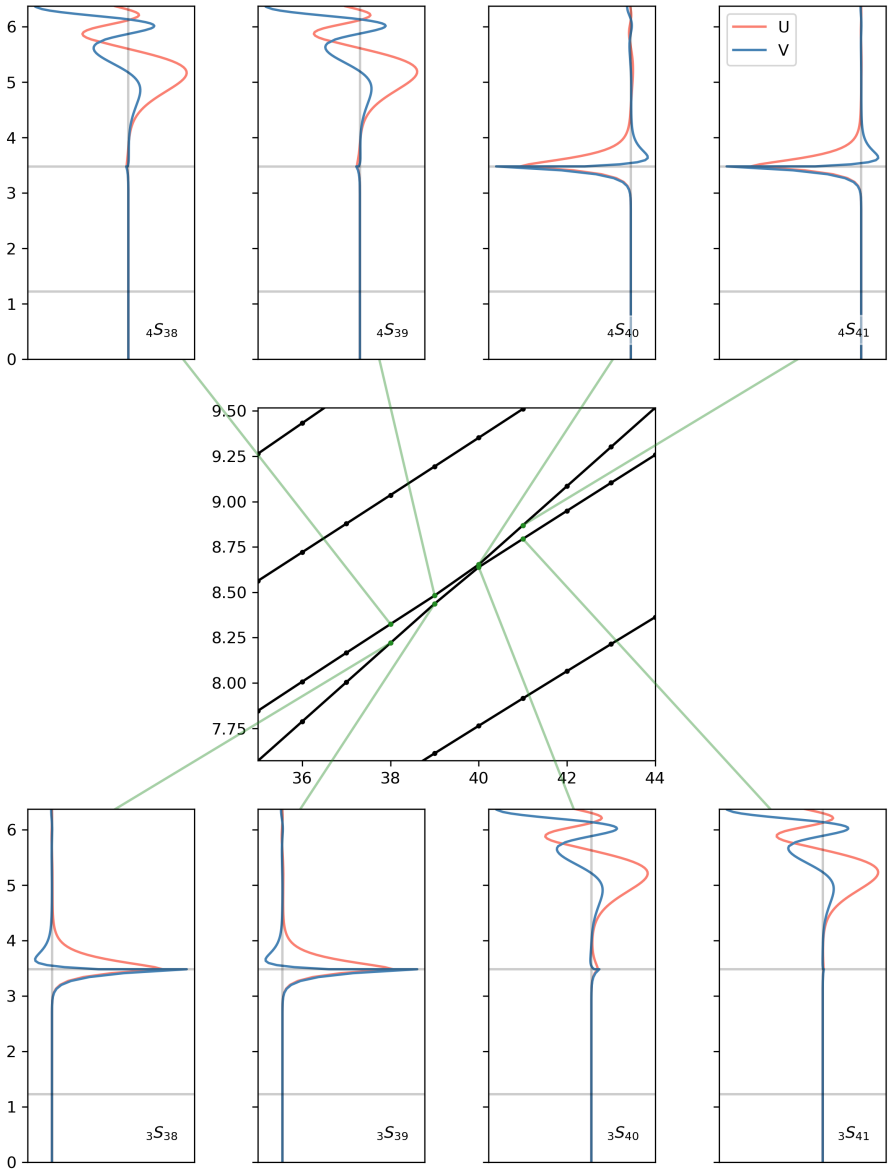

Figure S12: Same as Supp. Fig. S10, but for the third quasi-intersection.